





Surface carrier dynamics and diffusion in inorganic metal-halide perovskite filmsJanek Rieger , Jonas Hauner , Daniel Niesner , and Thomas Fauster ^{*}*Lehrstuhl für Festkörperphysik, Friedrich-Alexander-Universität Erlangen-Nürnberg (FAU), Staudtstrasse 7, 91058 Erlangen, Germany*

(Received 21 November 2022; revised 24 January 2023; accepted 24 February 2023; published 20 March 2023)

Carrier dynamics in metal-halide perovskites, in particular diffusion, has typically been investigated on micrometer-length scales and above. However, surfaces and interfaces modify the carrier dynamics, e.g., by interface band bending and recombination. To investigate the carrier dynamics and diffusion at the surface, we use time-resolved photoelectron spectroscopy which is sensitive to the photoexcited carriers in the topmost few nm of the material. We extract electron mobilities in well-ordered CsPbBr₃(001) and CsSnBr₃(001) films at room temperature of 31 ± 6 and 13 ± 1 cm² V⁻¹ s⁻¹, respectively. The mobility in CsPbBr₃(001) increases to 200 ± 8 cm² V⁻¹ s⁻¹ at 90 K, indicating strong electron-phonon coupling for electrons at the conduction band minimum. Temperature-dependent photoemission experiments find different phonon coupling mechanisms for high-energetic electrons and holes at the valence band maximum and in the main valence bands.

DOI: [10.1103/PhysRevB.107.125205](https://doi.org/10.1103/PhysRevB.107.125205)**I. INTRODUCTION**

Despite the intense research on metal-halide perovskites (MHP), a lot of basic material parameters such as the charge carrier mobility vary by orders of magnitude in different reports [1–3]. A reason for the huge spread could be the quality of investigated samples. Besides bulk defects, which are subject to intense research, surfaces and interfaces affect carrier dynamics and mobility. In general, surfaces with different orientations and terminations may have rather different effects on, e.g., band bending or surface recombination [4]. It is therefore critical to control the sample quality precisely. Furthermore, the spatial resolution, the probed time scale, carrier densities, and limitations of utilized experimental methods should be taken into account [1].

The control of sample quality is also an important factor when experiments aim for fundamental understanding. Charge carrier mobilities are limited by strong interaction of charge carriers and phonons in MHPs. However, the exact interaction mechanism is still debated [1]. Charge carriers in MHPs could be scattered by the acoustic deformation potential, by piezoelectric acoustic phonon scattering, or by Fröhlich interactions with polar optical phonons. Temperature-dependent mobility measurements are often performed to distinguish the different mechanisms [1,5,6]. Methylammonium-lead-iodide single crystals and polycrystalline films exhibit temperature-dependent mobilities $\mu_e \propto T^{-2.8}$ and $\propto T^{-1.6}$ around 300 K, respectively [2]. One limiting factor is that most of the performed experiments are not sensitive to the type and energy of the charge carriers. Both aspects may alter the measured temperature-dependent charge-carrier mobilities [1,2,7]. Well-defined samples as well as charge- and energy-sensitive experiments are needed for a better understanding.

Recently, we established a method to prepare inorganic CsPbBr₃ and CsSnBr₃ films with a well-defined (001) surface orientation [see Fig. 1(d)] [8]. Our samples exhibit highly ordered atomic surface structures and very low defect densities. Their thickness can be controlled precisely on the monolayer (ML) scale. This sets the stage to investigate fundamental electronic properties of MHPs. Ultraviolet photoelectron spectroscopy (UPS) was used to study valence bands and Fermi-level alignment at the interface. The dispersion of the valence bands was measured with angle-resolved photoelectron spectroscopy (ARPES) and the effective mass at the valence band maximum (VBM) is obtained. Time-resolved two-photon photoemission (2PPE) accesses the conduction bands with high temporal resolution of <75 fs and high surface sensitivity of <4 nm. This permits the investigation of charge carrier dynamics in the topmost layers of the material. Our detailed knowledge of the interface band bending, the band structure, and the extremely high quality of our samples enable an unprecedented study of the charge carrier mobilities in MHPs. Temperature-dependent measurements provide a new perspective on charge-phonon interaction in MHPs.

II. EXPERIMENT

Epitaxially grown CsPb(Sn)Br₃(001) films were prepared by thermal coevaporation of CsBr and Pb(Sn)Br₂ (all three Sigma-Aldrich, 99% purity) on a clean Au(001) substrate. Details of the preparation are described in Ref. [8]. Ultraviolet photoelectron spectroscopy was carried out using unpolarized light with a photon energy of 21.2 eV (He I). Satellite lines were subtracted for analysis. An optical parametric amplifier (Light Conversion Opera-F) pumped by a fiber laser (Coherent Monaco) was used to generate 880-nm laser pulses with pulse durations below 40 fs for 2PPE experiments. Second (2.82 eV) and third (4.23 eV) harmonics of the laser pulses were used for pump and probe, respectively. Their cross correlation was determined from the high-energetic tail of the

^{*}thomas.fauster@fau.de

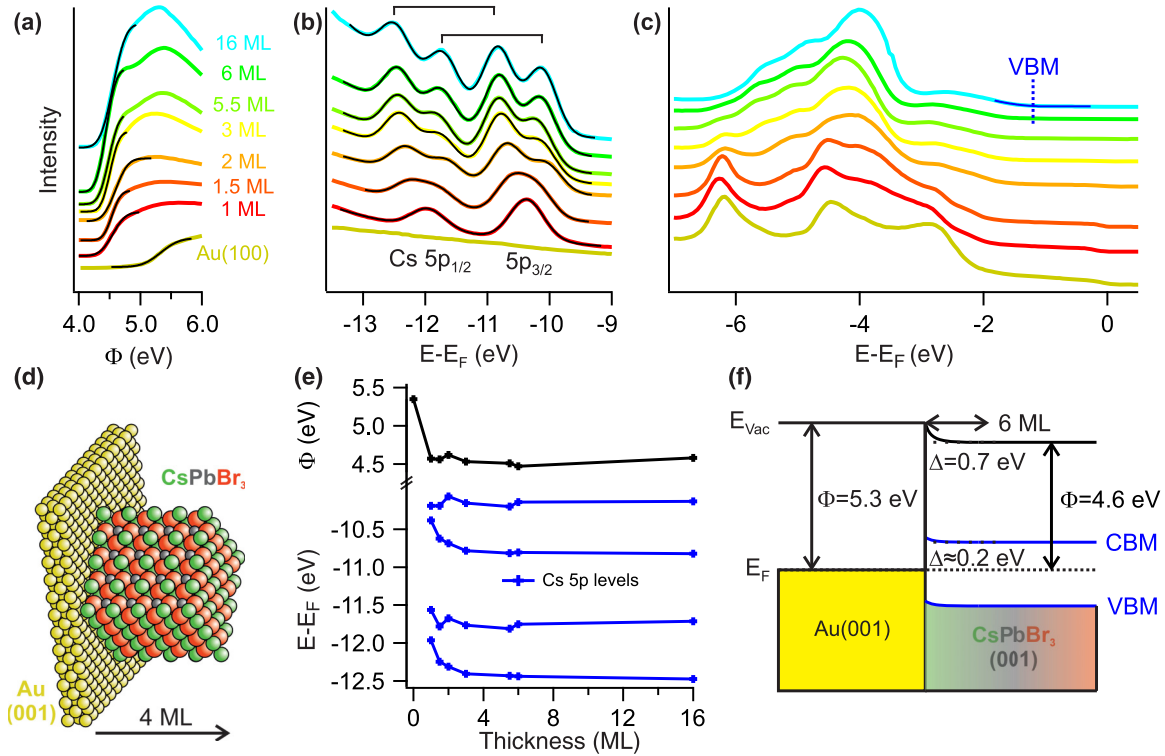


FIG. 1. Electronic structure of epitaxial CsPbBr₃(001) on Au(001) at 90 K with the crystal structure illustrated in panel (d). (a) Low-energy cutoff, (b) Cs 5p levels, and (c) the angle-integrated valence bands as a function of layer thickness. Colored lines show data and black lines the corresponding fits in panels (a) and (b), respectively. The energies from the fits of the Cs 5p doublet and the vacuum edge are shown in panel (e) and are used to obtain the band bending at the interface between Au(001) and CsPbBr₃ shown in panel (f).

2PPE spectra to 75 fs. The charge carrier density injected by the pump pulse is estimated to $\approx 1 \times 10^{17} \text{ e}^- \text{ cm}^{-3}$ for 1 nJ pulse energy [9].

Photoelectrons were measured with an ellipsoidal display-type analyzer [10]. It collects photoelectrons from an emission cone with an opening angle of 40° with respect to the surface normal. Its energetic and angular resolution is 100 meV and 5° , respectively. All photoelectrons from an emission cone with an opening angle of 25° with respect to the surface normal were integrated for shown UPS and 2PPE spectra.

III. VALENCE BANDS

A. Energy level alignment at the interface

Figure 1 shows the UPS spectra from films of different thickness at the low-energy cutoff, the Cs 5p levels, and the valence-band region. For film thicknesses up to 3 ML, the Au 4d bands can be clearly identified. For thicker films, the three-peak valence-band structure characteristic for MHPs develops [12]. To identify the work function and band alignment of the perovskites on gold, we extract the work function from the low-energy cutoff [Fig. 1(a)] by fitting error functions to the data (black lines). The energetic positions of the Cs 5p core levels [Fig. 1(b)] is used to identify the valence-band position relative to the Fermi energy E_F obtained on the clean Au substrate. Upon adsorption of CsPbBr₃ on Au(001), the work function Φ decreases from 5.3 ± 0.1 to 4.6 ± 0.1 eV. Saturation is achieved after 1 ML. The shallow Cs 5p core levels of CsPbBr₃ appear in the UPS spectra [Fig. 1(b)] at

energies between 9 and 13 eV below the Fermi energy E_F . They are split into a $5p_{1/2}$ and $5p_{3/2}$ doublet with a separation of 1.6 ± 0.1 eV. A single doublet is observed for 1 ML CsPbBr₃ on Au(001). When the film thickness of the MHP is increased beyond 1 ML a second doublet at higher energy is observed while the first doublet shifts to lower energy. The splitting into two components is characteristic for well-ordered MHPs and cannot be explained by bulk and surface components [8]. The splitting might be associated with several inequivalent Cs atoms in the bulk-terminated orthorhombic superstructure, which would require a detailed structural analysis to resolve.

In order to investigate the interface band bending, the two Cs 5p doublets were fitted with Voigt profiles. Details of the fitting procedure are given in the Supplemental Material [9]. Assuming that the energy of the Cs 5p levels are fixed relative to the valence bands, we obtain the energy of the VBM relative to the vacuum level as a function of film thickness [Fig. 1(e)]. The results are summarized in the band bending scheme in Fig. 1(f). The band bending of 0.2 eV for low coverages indicates a small interface dipole and associated charge transfer at the interface between the CsPbBr₃ film and the Au substrate. This result is in line with a study where Au was evaporated onto a MHP [13].

The results from epitaxial CsSnBr₃(001) on Au(001) are very similar [9]. Small band bending of 0.2 eV can be found between both MHPs and the substrate. CsSnBr₃ (001) also has a work function of $\Phi = 4.6 \pm 0.1$ eV, suggesting a CsBr termination for both MHPs prepared stoichiometrically [8].

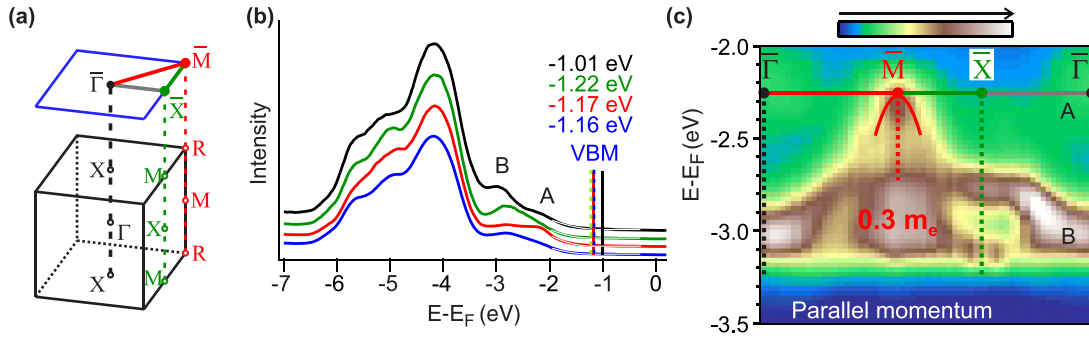


FIG. 2. Valence band dispersion of epitaxial CsPbBr₃(001) at 90 K. (a) Bulk and surface Brillouin zone of CsPbBr₃(001). The high-symmetry points $\bar{\Gamma}$, \bar{X} , and \bar{M} are indicated in black, green, and red. (b) Corresponding ARPES spectra at the high-symmetry points in comparison with the angle-integrated photoemission signal of the whole Brillouin zone (blue curve) for a 12.5-ML film. Thin white lines show half-parabola fits to obtain the VBM [11]. The dispersion of the topmost valence band with the main features A and B along $\bar{\Gamma}$ - \bar{M} - \bar{X} - $\bar{\Gamma}$ was pronounced by building the minimal gradient of the three-dimensional $I(E, k_x, k_y)$ ARPES data set and is presented in panel (c). As a guide to the eye, a parabola with a curvature of $0.3 m_e$ is plotted at the \bar{M} point.

The identical value for the band bending hints at a similar atomic and electronic structure at the interface, which makes a CsBr layer at the Au substrate for both systems plausible. Note that the PbBr₂ termination at the CsPbBr₃(001) surface has a work function 0.7 eV higher than the CsBr-terminated surface [8].

As compared to CsPbBr₃, CsSnBr₃ films [9] show a slightly smaller effective mass of $\approx 0.2 m_e$ in line with band-structure calculations [14,15]. The CsSnBr₃ thin films also show the VBM at \bar{M} and $\bar{\Gamma}$, with $E - E_F = -0.2 \pm 0.1$ eV. Tin-based MHPs are commonly p-doped [16] and the relative shift of the VBM in CsSnBr₃ with respect to CsPbBr₃ was also observed in CsPb_xSn_{1-x}Br₃ samples [17].

B. Valence band dispersion

The dispersion of the valence bands throughout the Brillouin zone obtained by ARPES is shown in Fig. 2. Spectra recorded at the high-symmetry points [Fig. 2(a)] for a 12.5-ML-thick film are shown in Fig. 2(b). The spectra are independent of the film thickness when it exceeds 6 ML. An angle-integrated valence band spectrum is shown in blue for comparison. All spectra show a three-peak structure with negligible dispersion at energies between -4 and -6 eV. Peaks A and B at higher energies reflect the topmost valence band. To accentuate the dispersion, a minimum gradient method was applied to the three-dimensional $I(E, k_x, k_y)$ data set [18]. The result is shown in Fig. 2(c) for the high-symmetry lines along the $\bar{\Gamma}$ - \bar{M} - \bar{X} - $\bar{\Gamma}$ path in the surface Brillouin zone. The main valence band [brown-white shading, feature B at $\bar{\Gamma}$ in Fig. 2(b)] disperses with its maximum at the \bar{M} point and can be described by an effective (hole) mass of $0.3 m_e$ [red parabola in Fig. 2(c)]. The VBM is expected for MHPs in the cubic bulk phase at \bar{M} due to the projection of the bulk VBM at the R point [see Fig. 2(a)]. A second dispersing band with lower intensity has its maximum at $\bar{\Gamma}$ [feature A at $\bar{\Gamma}$ in Fig. 2(b)]. Its dispersion resembles the one of the main valence band, but mirrored at the perpendicular bisector of $\bar{\Gamma}$ - \bar{M} [green shade in Fig. 2(c)]. We assign it to a back-folded band from the bulk-terminated orthorhombic superstructure [9]. Therefore, the global VBM can be determined at the \bar{M} point as well as the $\bar{\Gamma}$ point. It is obtained at $E - E_F = -1.2 \pm 0.1$ eV from a

half-parabola fit [8,11,19] to the high-energy tails of the spectra. Considering the optical band gap of CsPbBr₃ of 2.25 eV [20], our epitaxial thin films are close to intrinsic. The negligible doping points toward a low-defect density consistent with our observations by scanning tunneling microscopy [8]. A fit to the high-energy part of the angle-integrated spectrum [blue curve in Fig. 2(b)] with a half parabola (white line) gives a similar energy of the VBM. This shows that angle-integrated photoemission spectra can be utilized to detect the global VBM of MHPs as proposed before [21]. The effective mass at the VBM could not be extracted from half-parabola fits presumably due to umklapps on the reconstructed films. It is assumed to be $\approx 0.3 m_e$ as obtained for peak A following previous work on cleaved samples which show no umklapp features [11,22].

IV. UNOCCUPIED STATES

A. Energies of conduction bands

We investigated the energetics and dynamics of photoexcited electrons in the conduction band with 2PPE. For 2PPE we use a blue (photon energy 2.82 eV, light blue arrows in Fig. 3) pump laser pulse to excite electrons from the occupied part of the band structure to unoccupied intermediate states. An ultraviolet (UV) laser pulse (4.23 eV, purple arrows) probes the electron distribution in the intermediate states after a controlled delay time t , thus tracking the electron dynamics on ultrafast time scales. The cross correlation of the two laser pulses was below 75 fs. The pump pulse excites an electron density of $\approx 8 \times 10^{17} \text{ e}^- \text{ cm}^{-3}$ [9].

Figure 3(a) shows 2PPE spectra at a time delay of 750 fs and Fig. 3(b) illustrates the possible excitation pathways. In Fig. 3(a), a UPS spectrum ($E - E_F < 0$ eV, blue) is shown for comparison. 2PPE was performed on thicker films (>12 ML) to ensure a sufficient lifetime of the photoexcited electrons (cf. Sec. IV B). Figure 3(a) shows 2PPE spectra recorded with high pump fluence (red) and low pump fluence (green). Note that the spectra are normalized to the same maximum height. The high-energy part of the 2PPE spectra can be excited only by the UV photons. Multiplying the high-pump-fluence spectrum by a factor of 10 gives about the same intensity

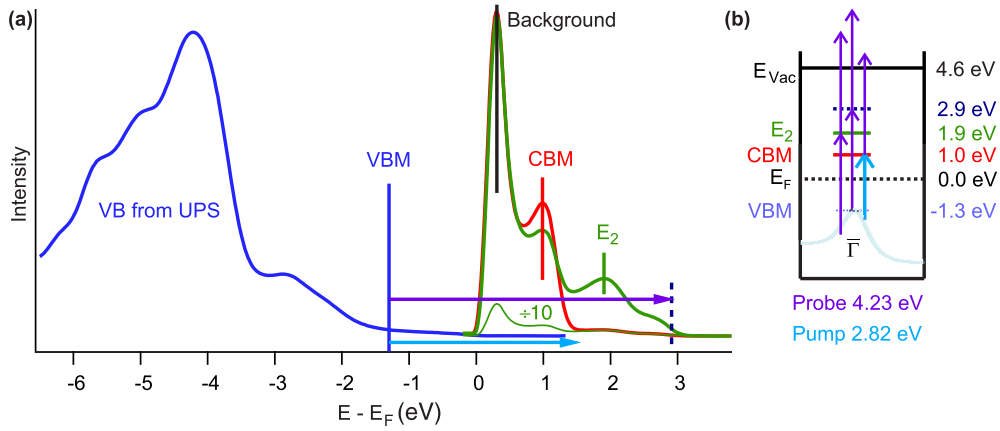


FIG. 3. Unoccupied states of CsPbBr₃ on Au(001). (a) UPS spectrum from 12 ML at 90 K (blue curve) for the valence bands and two bichromatic 2PPE spectra with different laser pulse energies from 45 ML at 295 K. The red (green) spectrum was recorded with 1.10 nJ (0.37 nJ) pump and 0.13 nJ (0.36 nJ) probe pulse energy. The spectra are normalized to the same maximum peak height. The low-pump spectrum is additionally shown scaled down by a factor of 10, illustrating the coincidence with the high-pump spectrum in the energy range excited by the UV probe photons only. The positions of all detected states VBM, CBM, and E_2 are marked by vertical bars. (b) Schematic band structure of CsPbBr₃ resulting from the ARPES and 2PPE experiments. The dispersion stems from Fig. 2(c). Possible excitation pathways in 2PPE are shown in panels (a) and (b) by arrows.

in the high-energy region as for low pump fluence. The factor is close to the intensity ratio of the pump fluences (8.5) and proves that the low-energy background is predominantly caused by the pump pulse.

Several features can be identified in the 2PPE spectra. The most intense peak at the lowest energy stems from the background caused by secondary electrons and one-photon photoemission of thermally excited photoelectrons. Another feature is located at $E - E_F = 1.0$ eV with high intensity for high pump pulse energy. It has an energetic separation from the VBM of 2.2 eV matching the optical band gap of CsPbBr₃ [20]. We assign it to the conduction band minimum (CBM). The third feature labeled E_2 is measured at $E - E_F \approx 1.9$ eV. This feature is both pumped and probed by UV photons and is observed only for UV photon energies higher than 3.45 eV (see Supplemental Material [9]). It corresponds to a transition between the valence and conduction band edges at the M point of the bulk Brillouin zone which is frequently observed as a second absorption onset in optical spectroscopy [5,23]. Finally, the highest energy electrons in the 2PPE spectra occur at $E - E_F \approx 2.9$ eV corresponding to a direct excitation from the VBM at -1.2 ± 0.1 eV by 4.23-eV photons and is marked by dashed lines in Fig. 3.

It was not possible to resolve any dispersion of the intermediate states with 2PPE. Possible explanations could be that the intermediate states are strongly broadened by dynamic disorder or that the probed states are localized.

For epitaxial CsSnBr₃(001), similar results are found by 2PPE [9]. CBM and E_2 are located at $E - E_F = 2.1 \pm 0.1$ eV and 2.7 ± 0.1 eV, respectively. The resulting band gap of 2.3 ± 0.2 eV is slightly larger than the recombination gap of 1.8 eV measured with photoluminescence [24].

B. Electron dynamics

Figure 4(a) shows the dynamics of the conduction band electrons. Notably, the pump photon energy is sufficiently

small to excite electrons (and holes) in the first conduction band (valence band) only. The conduction band electrons exhibit two distinct time scales which can be distinguished by different dependencies on the film thickness. The shorter time constant τ_1 is in the femtosecond time range and does not depend on the film thickness. Its weighted mean value is $\tau_1 = 160 \pm 10$ fs for all investigated films. This ultrafast time constant is caused by nascent high-energetic electrons and was previously assigned to the formation of large polarons or to the ballistic transport of charge carriers [25–29].

The second time constant τ_2 of several picoseconds depends quadratically on film thickness [Fig. 4(b)] so that it can be assigned to the diffusion of electrons out of the probed volume. Figure 4(c) illustrates our model of the process. In 2PPE, the escape depth of electrons is < 4 nm. Thus we only probe the electron density $n(0, t)$ at the surface ($x = 0$). CsPbBr₃ has an absorption length on the order of 75 nm for the used pump photon energy of 2.82 eV [23], which is larger than the thickness (50 nm) of the thickest film (90 ML) studied. Therefore, the pump pulse excites a constant charge carrier density n_0 at $t = 0$ in the whole film. Thereafter ($t > 0$), charge carriers diffuse with a diffusion constant D . Charge carriers are lost at the interface to the metallic substrate. The resulting gradient of the charge carrier density $n(x, t)$ causes a diffusion of charge carriers from the film to the gold substrate. As a result, the charge carrier density at the surface decays exponentially with time. The diffusion constant D can be determined from the decay times of the charge carrier density at the surface by solving the corresponding one-dimensional differential equation:

$$\frac{\partial n}{\partial t} = D \frac{\partial^2 n}{\partial x^2}. \quad (1)$$

We neglect (surface) recombination expected on time scales > 100 ns resulting in an isolated surface as one of the boundary conditions. The second boundary condition is that the charge carrier density at the gold substrate is zero. The detailed

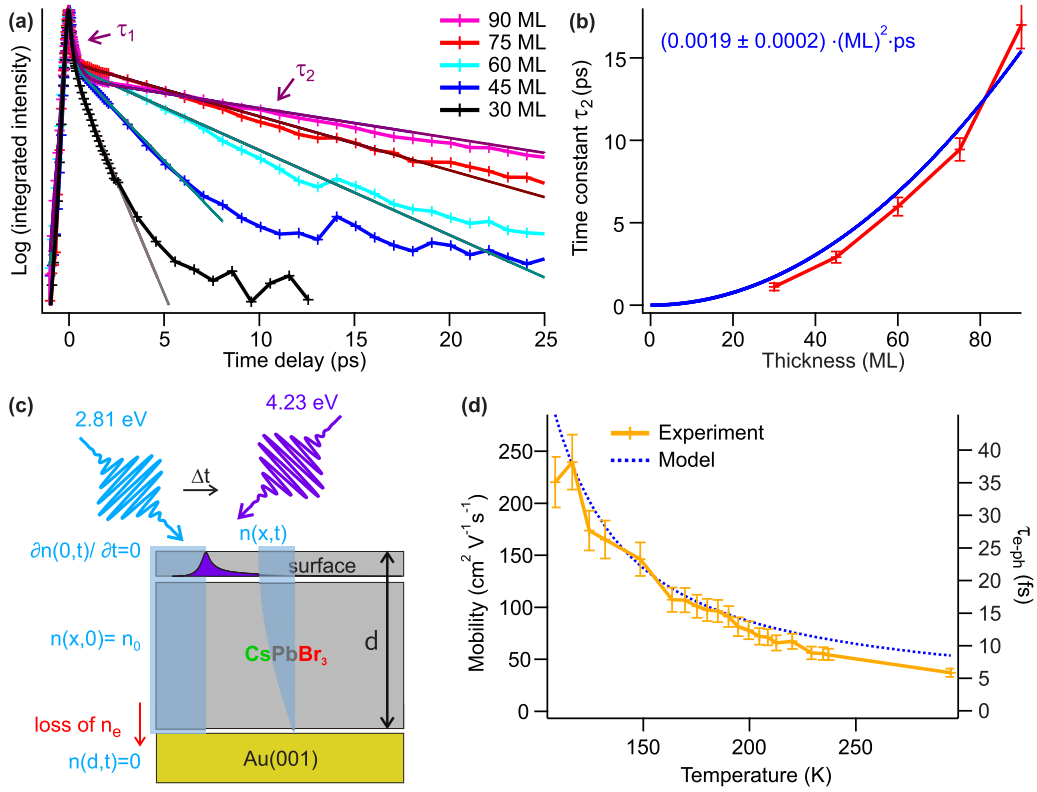


FIG. 4. Dynamics of excited electrons in CsPbBr₃(001). (a) Angle- and energy-integrated 2PPE intensities at varying pump-probe delay from films with thickness between 30 and 90 ML measured at room temperature and corresponding bi-exponential fits to the data. The extracted time constant τ_2 is plotted against the film thickness d in panel (b) and fitted with a parabola. (c) Model used to describe the thickness-dependent behavior of τ_2 and calculate the diffusion constant of excited electrons D from $\tau_2(d)$. (d) Temperature-dependent electron mobility $\mu_e(T)$ from 2PPE experiments on a 60-ML film together with a model [15].

solution of Eq. (1) is presented in the Supplemental Material [9]. The charge carrier density at the surface ($x = 0$) of a film with thickness d is described by

$$n(0, t) = \sum_{m=0}^{\infty} \frac{4n_0}{\pi} \left[\frac{1}{4m-3} e^{-\left(\frac{4m-3}{2d}\right)^2 Dt} - \frac{1}{4m-1} e^{-\left(\frac{4m-1}{2d}\right)^2 Dt} \right]. \quad (2)$$

Because of the rapidly decreasing amplitude of the higher order terms it is sufficient to evaluate the terms with $m \leq 2$ (see Supplemental Material [9]). For each thickness d the diffusion constant D is determined by fitting Eq. (2) to the measured 2PPE time dependence. The fits and results are presented in the Supplemental Material [9] and yield an averaged $D = 1.0 \pm 0.1 \text{ cm}^2 \text{ s}^{-1}$. The small scatter of D obtained from the individual time dependencies proves the validity of the diffusion model for the thickness-dependent electron dynamics. The electron mobility μ_e is obtained with the Nernst-Einstein relation $\mu_e(T) = eD/k_B T$ to $37 \pm 4 \text{ cm}^2 \text{ V}^{-1} \text{ s}^{-1}$ at room temperature. This value is in line with most of the studies on MHPs, but orders of magnitude lower than in group IV and III-V semiconductors [5].

CsSnBr₃ exhibits $\mu_e(295 \text{ K}) = 13 \pm 3 \text{ cm}^2 \text{ V}^{-1} \text{ s}^{-1}$ [9]. The low mobility in MHPs is typically ascribed to phonon scattering. Due to the lower effective mass of charge carriers

one would expect higher electron mobilities in CsSnBr₃ [15]. The discrepancy with our results may stem from a higher defect density in CsSnBr₃.

C. Electron-phonon coupling

To further test the influence of electron-phonon scattering, temperature-dependent 2PPE measurements were carried out for CsPbBr₃. The longer decay time $\tau_2(T)$ increases linearly with temperature [9]. Figure 4(d) presents the resulting temperature-dependent electron mobility which was determined from $\tau_2(T)$ starting with $\mu_e(295 \text{ K}) = 37 \text{ cm}^2 \text{ V}^{-1} \text{ s}^{-1}$. The electron mobility μ_e approximately follows a power-law dependence $T^{-\beta}$ on temperature approaching a T^{-2} dependence at low temperatures. No impact of defect-induced scattering is observed at lower temperatures, which would reduce the mobility. Electron-phonon scattering is clearly the most dominant process. Figure 4(d) compares our experimental results with a theoretical model (blue dotted curve) [15]. The model assumes just the interaction of electrons with the highest optical phonon mode ($\hbar\omega_{LO} = 16.8 \text{ meV}$) [27,30]. It is in excellent agreement with our data, indicating that scattering of electrons at the CBM is dominated by the highest optical phonons caused by PbBr₃ stretching modes [15]. These findings are also in line with results from optical spectroscopy in which a dominant coupling of

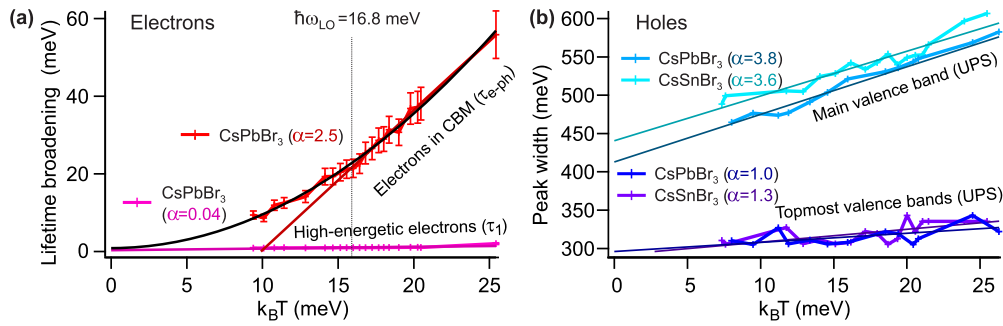


FIG. 5. Temperature-dependent photoemission linewidths. (a) Linewidths of intermediate states which were modeled from the time constants τ_1 and τ_{e-ph} measured with 2PPE. (b) UPS peak widths of the main valence band (light blue) and the topmost valence bands (blue and violet) in CsPbBr₃ and CsSnBr₃, respectively.

electrons at the CBM to PbBr₃⁻ stretching modes was found [7]. Electron-phonon scattering times were determined with the Drude model: $\tau_{e-ph}(T) = \mu_e(T) \frac{m_e^*}{e} \propto T^{-\beta}$ assuming $m_e^* = m_h^* = 0.28 m_e$ [22]. The results show a drop of τ_{e-ph} between 100 K and 240 K of about 77 % [right axis in Fig. 4(d)]. Note that no signs for a phase transition such as an abrupt change of $T^{-\beta}$ are observed in the temperature-dependent mobility, which would indicate well-defined phase transition temperatures. This agrees with our study in which we observed no phase transitions and only gradual changes of the atomic surface structure of epitaxial CsPbBr₃(001) films with temperature [8].

We now turn to the evaluation of the ultrafast time-constant τ_1 obtained from the temperature-dependent 2PPE spectra. τ_1 was assigned to the relaxation of high-energetic electrons in the conduction band and decreases linearly with temperature (see Supplemental Material [9]). The overall decrease is only 20% between 100 K and 240 K. τ_1 cannot be associated with the diffusive transport of electrons away from the probed surface which would become slower with increasing temperature. Its weak temperature dependence indicates an interaction with phonons but the underlying interaction must be different from the electron-phonon scattering at the CBM, because the latter is influenced more strongly by temperature. One explanation for the weak temperature dependence of τ_1 could be the formation of large polarons on ultrafast time scales accompanied by a change of the photoionization cross section [25,27]. The formation of large polarons is related to the coupling of electrons with PbBr₃⁻ bending modes, while the charge carriers close to the band edges couple to PbBr₃⁻ stretching modes [31]. An increased temperature can lead to the faster formation of large polarons [7].

Temperature-dependent UPS was carried out to access also phonon-hole scattering for comparison with the electron scattering accessed by 2PPE. The lifetimes τ_{e-ph} and τ_1 from 2PPE were converted to energetic widths W using the relation $W = \hbar/\tau$ [32,33]. Note that time constant τ_2 corresponds to diffusion of electrons and must not be interpreted as a lifetime. Instead, the lifetimes of electrons at the CBM are estimated from the electron-phonon scattering times τ_{e-ph} . Long lifetimes can be measured very accurately and lead to small error bars (<10 meV) for the lifetime broadening in Fig. 5(a). With increasing temperature, lifetimes get shorter and the lifetime broadening and corresponding error increases. Fig-

ure 5 compares the modeled electron linewidths of CsPbBr₃ with the hole peak widths of CsPbBr₃ and CsSnBr₃ measured by UPS. The peak widths increase linearly as expected when the thermal energy exceeds the maximum phonon energy [33]. The maximum deviation of the experimental data points from the linear fits in Fig. 5(b) of less than 30 meV serves as an upper limit for the accuracy of the determination of the peak width. The lifetime broadening of the electrons at the CBM shows a parabolic behavior at low temperatures with a negligible offset, indicating very little contributions from defects or disorder. A change to a linear slope is observed above the energy of the highest optical phonon (16.8 meV). This energy was also used to model the temperature-dependent mobilities before [compare Fig. 4(d)]. Linear fits were applied to approximate the mass enhancement factor λ from the temperature-dependent peak widths $W(T) = 2\pi\lambda k_B T$ [34]. This allows a determination of the polaron coupling strength α from the relation $0.025\alpha^2 + \frac{1}{6}\alpha = \lambda$ [32]. The determined coupling strengths are given in Fig. 5.

Electrons and holes close to the band edges exhibit weak coupling strengths ($\alpha = 1 \dots 2.5$) consistent with large polarons and previous observations [6,15]. One implication is that the VBM must be renormalized by polaronic coupling as observed before but questioned recently [22,35,36]. The coupling strength for electrons at the CBM of CsPbBr₃ is about a factor of two higher than for holes at the VBM. Such behavior was observed before but is not evident from the band structure of MHPs [2]. Holes are expected to interact stronger than electrons with the relevant PbBr₃⁻ phonon modes since the VBM stems from Pb 6s and Br 4p orbitals [31]. High-energetic electrons with excess energies above the CBM show a smaller coupling strength in comparison to charge carriers at the band edges. This behavior is in line with screened electrons in large polarons as discussed before if τ_1 is assigned to a formation time [7]. On the other hand, if τ_1 would correspond to any kind of transport the corresponding scattering times would exhibit a $T^{-\beta}$ dependence. In contrast, high-energetic holes with excess energies of 3 eV below the VBM show different behavior. Their coupling strengths are large in both CsPbBr₃ and CsSnBr₃. They are much larger than typically assumed for large polarons in MHPs [22,32]. The large coupling strengths are rather in line with the formation of small polarons immediately after optical excitation [37–39].

V. SUMMARY AND CONCLUSIONS

Epitaxially grown CsPbBr₃(001) and CsSnBr₃(001) films on Au(001) allowed a detailed study of the electronic structure of inorganic MHPs. For both materials, a small band bending of 0.2 eV can be observed at the interface to the substrate. Films thicker than 6 ML exhibit a valence band structure consistent with the one of single crystals. The topmost valence bands disperse parabolically with an effective mass of $\approx 0.3 m_e$ and $\approx 0.2 m_e$, respectively. Their VBMs are located at $E - E_F = -1.2 \pm 0.1$ and -0.2 ± 0.1 eV, respectively. Both MHPs exhibit a back-folding of the main valence band, indicating an overall ($\sqrt{2} \times \sqrt{2}$) electronic superstructure. 2PPE experiments find the CBM of CsPbBr₃ at $E - E_F = 1.0 \pm 0.1$ eV so that epitaxial CsPbBr₃ films are intrinsic semiconductors. In contrast, CsSnBr₃ is strongly p doped and has its CBM at $E - E_F = 2.1 \pm 0.1$ eV.

Electrons in the CBM of CsPbBr₃ and CsSnBr₃ exhibit at room-temperature mobilities of 37 ± 4 and 13 ± 1 cm² V⁻¹ s⁻¹, respectively. The absolute values of the mobility in CsPbBr₃ as well as its temperature-dependence $\mu_e(T) \propto T^{-\beta}$ (approaching T^{-2} at low temperature) are in excellent agreement with a theoretical model taking into account only the interaction with the highest energetic polar phonon mode [15]. The relaxation of high-energetic electrons is less influenced by temperature possibly due to the formation of large polarons.

ACKNOWLEDGMENT

This work was funded by the Deutsche Forschungsgemeinschaft (DFG, German Research Foundation), Project No. 395604916.

-
- [1] L. M. Herz, Charge-carrier mobilities in metal halide perovskites: Fundamental mechanisms and limits, *ACS Energy Lett.* **2**, 1539 (2017).
- [2] S. Shrestha, G. J. Matt, A. Osvet, D. Niesner, R. Hock, and C. J. Brabec, Assessing temperature dependence of drift mobility in methylammonium lead iodide perovskite single crystals, *J. Phys. Chem. C* **122**, 5935 (2018).
- [3] T. J. Savenije, D. Guo, V. M. Caselli, and E. M. Hutter, Quantifying charge-carrier mobilities and recombination rates in metal halide perovskites from time-resolved microwave photoconductivity measurements, *Adv. Energy Mater.* **10**, 1903788 (2020).
- [4] C. Ma, M. Grätzel, and N.-G. Park, Facet engineering for stable, efficient perovskite solar cells, *ACS Energy Lett.* **7**, 3120 (2022).
- [5] L. M. Herz, Charge-carrier dynamics in organic-inorganic metal halide perovskites, *Annu. Rev. Phys. Chem.* **67**, 65 (2016).
- [6] L. R. Buizza and L. M. Herz, Polarons and charge localization in metal-halide semiconductors for photovoltaic and light-emitting devices, *Adv. Mater.* **33**, 2007057 (2021).
- [7] P. P. Joshi, S. F. Maehrlein, and X. Zhu, Dynamic screening and slow cooling of hot carriers in lead halide perovskites, *Adv. Mater.* **31**, 1803054 (2019).
- [8] J. Rieger, T. Kießlinger, A. Raabgrund, J. Hauner, D. Niesner, M. A. Schneider, and T. Fauster, Epitaxial inorganic metal-halide perovskite films with controlled surface terminations, *Phys. Rev. Mater.* **7**, 035403 (2023).
- [9] See Supplemental Material at <http://link.aps.org/supplemental/10.1103/PhysRevB.107.125205> for details of the experimental and methodical procedures as well as the data for CsSnPb₃, which includes Refs. [24,40–45].
- [10] D. Rieger, R. Schnell, W. Steinmann, and V. Saile, A display-type analyzer with an image-processing system for angle-resolved photoelectron spectroscopy, *Nucl. Instrum. Methods. Phys. Res.* **208**, 777 (1983).
- [11] D. Niesner, M. Wilhelm, I. Levchuk, A. Osvet, S. Shrestha, M. Batentschuk, C. Brabec, and T. Fauster, Giant Rashba Splitting in CH₃NH₃PbBr₃ Organic-Inorganic Perovskite, *Phys. Rev. Lett.* **117**, 126401 (2016).
- [12] S. Olthof, Research update: The electronic structure of hybrid perovskite layers and their energetic alignment in devices, *APL Mater.* **4**, 091502 (2016).
- [13] X. Liu, C. Wang, L. Lyu, C. Wang, Z. Xiao, C. Bi, J. Huang, and Y. Gao, Electronic structures at the interface between Au and CH₃NH₃PbI₃, *Phys. Chem. Chem. Phys.* **17**, 896 (2015).
- [14] P. Umari, E. Mosconi, and F. De Angelis, Relativistic GW calculations on CH₃NH₃PbI₃ and CH₃NH₃SnI₃ perovskites for solar cell applications, *Sci. Rep.* **4**, 4467 (2014).
- [15] S. Poncé, M. Schlipf, and F. Giustino, Origin of low carrier mobilities in halide perovskites, *ACS Energy Lett.* **4**, 456 (2019).
- [16] K. J. Savill, A. M. Ulatowski, and L. M. Herz, Optoelectronic properties of tin-lead halide perovskites, *ACS Energy Lett.* **6**, 2413 (2021).
- [17] H. A. Schwartz, H. Laurenzen, A. Marzouk, M. Runkel, K. O. Brinkmann, D. Rogalla, T. Riedl, S. Ashhab, and S. Olthof, Band-gap tuning in all-inorganic CsPb_xSn_{1-x}Br₃ perovskites, *ACS Appl. Mater. Interfaces* **13**, 4203 (2021).
- [18] Y. He, Y. Wang, and Z.-X. Shen, Visualizing dispersive features in 2D image via minimum gradient method, *Rev. Sci. Instrum.* **88**, 073903 (2017).
- [19] P. Schulz, D. Cahen, and A. Kahn, Halide perovskites: Is it all about the interfaces? *Chem. Rev.* **119**, 3349 (2019).
- [20] C. C. Stoumpos, L. Frazer, D. J. Clark, Y. S. Kim, S. H. Rhim, A. J. Freeman, J. B. Ketterson, J. I. Jang, and M. G. Kanatzidis, Hybrid germanium iodide perovskite semiconductors: Active lone pairs, structural distortions, direct and indirect energy gaps, and strong nonlinear optical properties, *J. Am. Chem. Soc.* **137**, 6804 (2015).
- [21] F. Zu, P. Amsalem, D. A. Egger, R. Wang, C. M. Wolff, H. Fang, M. A. Loi, D. Neher, L. Kronik, S. Duhm *et al.*, Constructing the electronic structure of CH₃NH₃PbI₃ and CH₃NH₃PbBr₃ perovskite thin films from single-crystal band structure measurements, *J. Phys. Chem. Lett.* **10**, 601 (2019).
- [22] M. Puppini, S. Polishchuk, N. Colonna, A. Crepaldi, D. N. Dirin, O. Nazarenko, R. DeGennaro, G. Gatti, S. Roth, T. Barillot, L. Poletto, R. P. Xian, L. Rettig, M. Wolf, R. Ernstorfer, M. V. Kovalenko, N. Marzari, M. Grioni, and M. Chergui, Evidence of Large Polarons in Photoemission Band Mapping of the

- Perovskite Semiconductor CsPbBr₃, *Phys. Rev. Lett.* **124**, 206402 (2020).
- [23] X. Chen, Y. Wang, J. Song, X. Li, J. Xu, H. Zeng, and H. Sun, Temperature-dependent reflectance and ellipsometry studies on a CsPbBr₃ single crystal, *J. Phys. Chem. C* **123**, 10564 (2019).
- [24] D. H. Fabini, G. Laurita, J. S. Bechtel, C. C. Stoumpos, H. A. Evans, A. G. Kontos, Y. S. Raptis, P. Falaras, A. Van der Ven, M. G. Kanatzidis *et al.*, Dynamic stereochemical activity of the Sn²⁺ lone pair in perovskite CsSnBr₃, *J. Am. Chem. Soc.* **138**, 11820 (2016).
- [25] D. Niesner, H. Zhu, K. Miyata, P. P. Joshi, T. J. Evans, B. J. Kudisch, M. T. Trinh, M. Marks, and X.-Y. Zhu, Persistent energetic electrons in methylammonium lead iodide perovskite thin films, *J. Am. Chem. Soc.* **138**, 15717 (2016).
- [26] Z. Chen, M.-i Lee, Z. Zhang, H. Diab, D. Garrot, F. Lédée, P. Fertey, E. Papalazarou, M. Marsi, C. Ponseca, E. Deleporte, A. Tejada, and L. Perfetti, Time-resolved photoemission spectroscopy of electronic cooling and localization in CH₃NH₃PbI₃ crystals, *Phys. Rev. Mater.* **1**, 045402 (2017).
- [27] T. J. Evans, K. Miyata, P. P. Joshi, S. Maehrlein, F. Liu, and X.-Y. Zhu, Competition between hot-electron cooling and large polaron screening in CsPbBr₃ perovskite single crystals, *J. Phys. Chem. C* **122**, 13724 (2018).
- [28] E. Jung, K. Budzinauskas, S. Öz, F. Ünlü, H. Kuhn, J. Wagner, D. Grabowski, B. Klingebiel, M. Cherasse, J. Dong, A. Pierfrancesco, P. Vivo, T. Kirchartz, T. Miyasaka, P. van Loosdrecht, L. Perfetti, and M. Sanjay, Femto- to microsecond dynamics of excited electrons in a quadruple cation perovskite, *ACS Energy Lett.* **5**, 785 (2020).
- [29] S. Polishchuk, Time- and angle-resolved photoelectron spectroscopy of solar materials, Ph.D. thesis, EPFL, Lausanne, Switzerland, 2021.
- [30] C. Wolf and T.-W. Lee, Exciton and lattice dynamics in low-temperature processable CsPbBr₃ thin-films, *Mater. Today Energy* **7**, 199 (2018).
- [31] K. Miyata, T. L. Atallah, and X.-Y. Zhu, Lead halide perovskites: Crystal-liquid duality, phonon glass electron crystals, and large polaron formation, *Sci. Adv.* **3**, e1701469 (2017).
- [32] M. Schlipf, S. Poncé, and F. Giustino, Carrier Lifetimes and Polaronic Mass Enhancement in the Hybrid Halide Perovskite CH₃NH₃PbI₃ From Multiphonon Fröhlich Coupling, *Phys. Rev. Lett.* **121**, 086402 (2018).
- [33] P. Hofmann, I. Y. Sklyadneva, E. D. L. Rienks, and E. V. Chulkov, Electron-phonon coupling at surfaces and interfaces, *New J. Phys.* **11**, 125005 (2009).
- [34] B. A. McDougall, T. Balasubramanian, and E. Jensen, Phonon contribution to quasiparticle lifetimes in Cu measured by angle-resolved photoemission, *Phys. Rev. B* **51**, 13891 (1995).
- [35] F. Reinert and S. Hüfner, Photoemission spectroscopy—from early days to recent applications, *New J. Phys.* **7**, 97 (2005).
- [36] M. Sajedi, M. Krivenkov, D. Marchenko, J. Sánchez-Barriga, A. K. Chandran, A. Varykhalov, E. D. L. Rienks, I. Aguilera, S. Blügel, and O. Rader, Is There a Polaron Signature in Angle-Resolved Photoemission of CsPbBr₃? *Phys. Rev. Lett.* **128**, 176405 (2022).
- [37] A. Marronnier, H. Lee, B. Geffroy, J. Even, Y. Bonnassieux, and G. Roma, Structural instabilities related to highly anharmonic phonons in halide perovskites, *J. Phys. Chem. Lett.* **8**, 2659 (2017).
- [38] C. Gehrman and D. A. Egger, Dynamic shortening of disorder potentials in anharmonic halide perovskites, *Nat. Commun.* **10**, 3141 (2019).
- [39] F. Wang, Y. Fu, M. E. Ziffer, Y. Dai, S. F. Maehrlein, and X.-Y. Zhu, Solvated electrons in solids—ferroelectric large polarons in lead halide perovskites, *J. Am. Chem. Soc.* **143**, 5 (2021).
- [40] M. Schmid, H.-P. Steinrück, and J. M. Gottfried, A new asymmetric pseudo-Voigt function for more efficient fitting of XPS lines, *Surf. Interface Anal.* **46**, 505 (2014).
- [41] D. Niesner, Surface electronic structure and dynamics of lead halide perovskites, *APL Mater.* **8**, 090704 (2020).
- [42] M.-I. Lee, A. Barragán, M. N. Nair, V. L. Jacques, D. Le Bolloc’h, P. Fertey, K. Jemli, F. Lédée, G. Trippé-Allard, E. Deleporte *et al.*, First determination of the valence band dispersion of CH₃NH₃PbI₃ hybrid organic-inorganic perovskite, *J. Phys. D: Appl. Phys.* **50**, 26LT02 (2017).
- [43] J. Yang, M. Meissner, T. Yamaguchi, B. Xi, K. Takahashi, S. A. Abd. Abdullah, X. Liu, H. Yoshida, M. Fahlman, and S. Kera, Temperature-dependent band structure evolution determined by surface geometry in organic halide perovskite single crystals, *Phys. Rev. B* **102**, 245101 (2020).
- [44] E. Mosconi, T. Etienne, and F. De Angelis, Rashba band splitting in organohalide lead perovskites: Bulk and surface effects, *J. Phys. Chem. Lett.* **8**, 2247 (2017).
- [45] H. Zhu, M. T. Trinh, J. Wang, Y. Fu, P. P. Joshi, K. Miyata, S. Jin, and X.-Y. Zhu, Organic cations might not be essential to the remarkable properties of band edge carriers in lead halide perovskites, *Adv. Mater.* **29**, 1603072 (2017).